Optical flow estimation of the heart's short axis view using a perceptual approach

Ernesto Moya-Albor[a,b], Boris Escalante-Ramírez[b] and Enrique Vallejo[c];

[a] Fac. de Ingeniería, Universidad Panamericana, Augusto Rodin 498, 03920 México, D.F.
[b] Fac. de Ingeniería, Dep. de Procesamiento de Señales, Edif. de Posgrado e Investigación,
[c] Fac. de Medicina, Unidad PET/CT Ciclotron, Nuevo Edif. de Investigación PB.
Universidad Nacional Autónoma de México, Cd. Universitaria, 04510 México, D.F.

ABSTRACT

This article describes a perceptual approach to calculate the optical flow estimation of the left ventricle in a short axis view of the heart in computer tomography images. The method is based on the the Hermite transform which is an image representation model that incorporates some of the more important properties of the first stages of the human visual system.

Our optical flow estimation approach incorporates a differential method that uses the steered Hermite coefficients as local constraints and uses the implicit multiresolution scheme of the Hermite transform to compute large displacements. It also involves several of the constraints seen in the current differential methods which allows obtaining an accurate optical flow.

We use the anatomic short axis view of the heart to calculate the optical flow estimation instead of the original computer tomography images of the axial plane. This view allows visualizing the left ventricle like a circular structure, which is more suitable for visualization of the left ventricle motion.

Keywords: Optical flow, differential method, steered Hermite transform, heart's short axis view, perceptual approach, heart's motion

1. INTRODUCTION

Congestive heart failure has increased worldwide due to both left ventricular and right ventricular failure. In the United States, about 5 million patients suffer from this problem and about 500,000 patients develop this condition each year. Previously it was due to the left ventricle (LV) pumping blood inefficiently (systolic ventricular failure). More recently, there has been emphasis on diastolic ventricular failure, where the systolic function appears to be normal, but diastolic ventricular function is impaired, being the cause of 50% of congestive heart failure in these patients. In order to develop better treatments for congestive heart failure, it is necessary to first understand the basic physiology and movement of both normal and abnormal ventricular relaxation and contraction.[1]

Understanding the movement of certain structures such as left ventricle and myocardial wall is fundamental for better medical diagnosis. This article describes a method to estimate the left ventricle's motion in computed tomography (CT) images. The left ventricle is the principal part of analysis for cardiac images due to the fact that it presents the most vital function of the heart.

In order to analyze the image sequence we perform a decomposition of the images into visual patterns that are relevant to the human vision system (HVS), such as directional edges, textures, etc. The Hermite transform[2,3] mimics some of the more important properties of early vision such as local processing and the Gaussian derivative models of receptive fields.[2–4] A rotated version of the Hermite transform provides a very efficient representation of oriented patterns which enables an adaptation to local orientation content at each window position over the image, indicating the direction of one–dimensional pattern.

Send correspondence to E.M.A.
E.M.A.: E–mail: emoya@up.edu.mx, Telephone: +52 55 5482 1600 Ext. 5210
B.E.R.: E-mail: boris@servidor.unam.mx,
E.V.: E-mail: vallejo.enrique@gmail.com

IX International Seminar on Medical Information Processing and Analysis, edited by
Jorge Brieva, Boris Escalante-Ramírez, Proc. of SPIE Vol. 8922, 892206 · © 2013
SPIE · CCC code: 0277-786X/13/$18 · doi: 10.1117/12.2041960

Since the heart is constantly in motion a temporal analysis is required, in this regard we use a differential approach to optical flow estimation using the Hermite transform,[5] which involves several of the constraints seen in the current differential methods, which allows obtaining an accurate optical flow like local image constraints, flow piecewise smooth, robust optimization functions and a multiresolution strategy.

In this work, the tomographic studies were analyzed using the short axis view of the heart, which is one of the three standard planes of the heart, this is due to the fact that the heart is oriented obliquely in the chest and the original CT images of the axial plane are suboptimal to visualize cardiac anatomy and pathology.

This paper is structured as follows. In Section 2 we present the theory and the mathematical foundations of the Hermite transform. The optical flow estimation method used is shown in Section 3, which includes elements that allow obtaining a robust optical flow in a perceptual framework. The results obtained in CT images are reported in Section 4 and conclusions are given in Section 5.

2. THE HERMITE TRANSFORM

The Hermite transform[2,3] is a special case of polynomial transform, it can be considered as an image description model. In order to calculate the Hermite transform, the original image $L(x, y)$ (where (x, y) are the coordinates of the pixels) is located at various positions multiplying $L(x, y)$ by the window function $v^2(x - x_0, y - y_0)$ at positions (x_0, y_0) that conform the sampling lattice S:

$$L_v(x - x_0, y - y_0) = L(x, y)v^2(x - x_0, y - y_0) \tag{1}$$

By replicating the window function over the sampling lattice, we can define a weight function different from zero for all (x, y):

$$V(x, y) = \sum_{(x_0,y_0)\in S} v^2(x - x_0, y - y_0) \tag{2}$$

Therefore the original image is represented within the window by:

$$L(x, y) = \frac{1}{V(x, y)} \sum_{(x_0,y_0)\in S} L(x, y)v^2(x - x_0, y - y_0) \tag{3}$$

The local information for each analysis window $L_v(x-x_0, y-y_0)$ is expanded in terms of a family of orthogonal polynomials $G_{m,n-m}(x, y)$ where $(n - m)$ and m denote the analysis order in x and y direction respectively.

$$L_{m,n-m}(x_0, y_0) = \int_{-\infty}^{\infty}\int_{-\infty}^{\infty} \left[L(x, y)v^2(x - x_0, y - y_0)\right] G_{m,n-m}(x - x_0, y - y_0)\, dxdy \tag{4}$$

The polynomials $G_{m,n-m}(x, y)$ used to approximate the information within the window are determined by the analysis window and satisfy the orthogonality condition:

$$\int_{-\infty}^{\infty}\int_{-\infty}^{\infty} v^2(x, y)G_{m,n-m}(x, y)G_{l,k-l}(x, y)\, dxdy = C_{nk}\delta_{nk}\delta_{ml} \tag{5}$$

for $n, k = 0, \ldots, \infty$, $m = 0, \ldots, n$ and $l = 0, \ldots, k$; where δ_{nk} denotes the Kronecker function ($\delta_{nk} = 1$ for $n = k$ and $\delta_{nk} = 0$ for $n \neq k$) and C_{nk} is a normalization factor.

The polynomials $G_{m,n-m}(x, y)$ are orthogonal with respect to the window function. From a perceptual point of view, adjacent Gaussian windows separated by twice the standard deviation σ are a good model of the overlapping receptive fields found in physiological experiments[6] and according to the scale–space theory,[7] our option would be a Gaussian window:

$$v(x, y) = \frac{1}{\sigma\sqrt{\pi}} \exp\left(-\frac{(x^2 + y^2)}{2\sigma^2}\right) \tag{6}$$

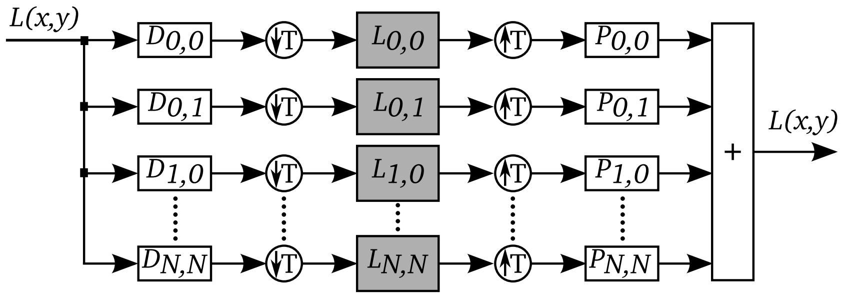

Figure 1. Analysis and synthesis process of the Hermite transform.

where the normalization factor defines a unitary energy for $v^2(x, y)$.

With a Gaussian window function, the associated orthogonal polynomials are the Hermite polynomials:[8]

$$G_{m,n-m}(x,y) = \frac{1}{\sqrt{2^n m!(n-m)!}} H_m\left(\frac{x}{\sigma}\right) H_{n-m}\left(\frac{y}{\sigma}\right) \tag{7}$$

where $H_n\left(\frac{x}{\sigma}\right)$ represents the generalized Hermite polynomials with respect to the Gaussian function (with variance σ^2) given by Rodrigues' formula:

$$H_n\left(\frac{x}{\sigma}\right) = (-1)^n \exp\left(-\frac{x^2}{\sigma^2}\right) \frac{d^n}{dx^n} \exp\left(-\frac{x^2}{\sigma^2}\right) \tag{8}$$

Thus, from Eq. (4) the Hermite coefficients $L_{m,n-m}(x, y)$ are calculated by a convolution of the original image $L(x, y)$ with the filter function $D_{m,n-m}(x, y)$, followed by a subsampling (T) at position (x_0, y_0) of the sampling lattice S (analysis process Fig. 1):

$$L_{m,n-m}(x_0, y_0) = \int_{-\infty}^{\infty} \int_{-\infty}^{\infty} L(x,y) D_{m,n-m}(x - x_0, y - y_0)\, dxdy \tag{9}$$

where $D_{m,n-m}(x, y) = G_{m,n-m}(-x, -y)v^2(-x, -y)$ and $n = 0, 1, \ldots, \infty$, $m = 0, 1, \cdots, n$.

The filter functions $D_{m,n-m}(x, y) = D_m(x)D_{n-m}(y)$ are separable because the Gaussian window is rotationally symmetric. The Hermite filters can be computed by:

$$D_n(x) = \frac{(-1)^n}{\sqrt{2^n n!}} \frac{1}{\sigma\sqrt{\pi}} H_n\left(\frac{x}{\sigma}\right) \exp\left(-\frac{x^2}{\sigma^2}\right) \tag{10}$$

Fig. 2 (left) shows the Hermite filters $D_{m,n-m}(x, y)$ for $N = 3$ ($n = 0, 1, \ldots, N$ and $m = 0, 1, \cdots, n$).

The analysis functions of the Hermite transform are similar to Gaussian derivatives, which, as argued before, are good models of some of the important retinal and cortical cells of the HSV,[4,9–12] where the retina responds to changes of light and not directly to light, this indicates that the eye works like a spatial differentiator of the scene *. The Gaussian derivatives model filter operations in human vision with the same accuracy as the Gabor filters, with the advantage that they accomplish this task with fewer parameters.[2,4,12] The free parameters are the maximum derivative order N, the subsampling factor T and the scale σ which must be related to the spatial scale of the image structures to be analyzed. Small windows are better to detect fine details and large windows allow analyzing low resolution objects. The Hermite transform has a multiresolution extension that allows analyzing objects at different scales.[13,14]

*The ganglion cells are known to be spot detectors that have receptive fields that look like $[-1 \quad 2 \quad 1]$ or $[1 \quad -2 \quad 1]$ so that they sense the local second derivative. The ganglion cells are involved in color vision, they compare signals from many different cones.

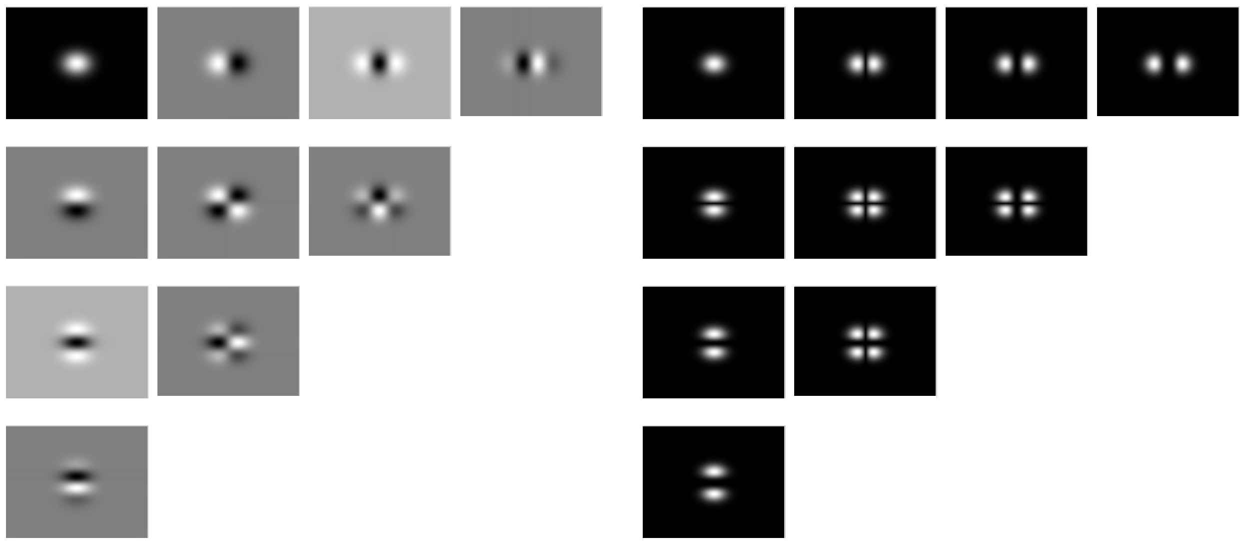

Figure 2. The Hermite filters $D_{m,n-m}(x,y)$ for $N = 3$ (left) and their Fourier transform spectrum (right) for $N = 3$ ($n = 0, 1, \dots, N$ and $m = 0, 1, \cdots, n$).

$$\begin{bmatrix} D_{0,0} & D_{1,0} & D_{2,0} & D_{3,0} \\ D_{0,1} & D_{1,1} & D_{2,1} & \\ D_{0,2} & D_{1,2} & & \\ D_{0,3} & & & \end{bmatrix}(x,y) \qquad \begin{bmatrix} d_{0,0} & d_{1,0} & d_{2,0} & d_{3,0} \\ d_{0,1} & d_{1,1} & d_{2,1} & \\ d_{0,2} & d_{1,2} & & \\ d_{0,3} & & & \end{bmatrix}(\omega_x,\omega_y)$$

In order to recover the original image, an interpolation of the transform coefficients with the synthesis filters $P_{m,n-m}(x,y) = \frac{G_{m,n-m}(x,y)v^2(x,y)}{V(x,y)}$ for $n = 0, \dots, \infty$ and $m = 0, \dots, n$ is performed followed by an oversampling and adding all the elements (synthesis process Fig. 1):

$$\hat{L}(x,y) = \sum_{n=0}^{\infty} \sum_{m=0}^{n} \sum_{(x_0,y_0)\in S} L_{m,n-m}(x_0,y_0) P_{m,n-m}(x-x_0, y-y_0) \tag{11}$$

Fig. 3 (left) shows the cartesian decomposition of the Hermite transform for $N = 3$ ($n = 0, 1, 2, 3$) for the slice 52 of the CT sequence at 20% of the cardiac cycle.

2.1 Steered Hermite transform

Oriented filters are a class of filters that are rotated copies of each filter, constructed as a linear combination of a set of basis filters.[15] The orientation feature of the Hermite filters explains why they are products of polynomials with a radially symmetric window function (Gaussian function). The $N + 1$ Hermite filters of order n form a steerable basis for each individual filter of order n. Because of this characteristic, Hermite filters at each position in the image are adapted to local content.[16] The resulting filters can be interpreted as directional derivatives of a Gaussian function. In this way, a more general expression of the $L_{m,n-m}$ cartesian Hermite coefficients can be written in terms of the orientation selectivity:

$$l_{m,n-m,\theta}(x_0,y_0) = \sum_{k=0}^{n} \Big(L_{k,n-k}(x_0,y_0)\Big)\Big(g_{k,n-k}(\theta)\Big) \tag{12}$$

where $l_{m,n-m,\theta}(x_0,y_0)$ are the steered Hermite coefficients and $g_{m,n-m}(\theta)$ are the cartesian angular functions of order n that expresses the directional selectivity of the filter:

$$g_{m,n-m}(\theta) = \sqrt{\binom{n}{m}}\Big(\cos^m(\theta)\Big)\Big(\sin^{n-m}(\theta)\Big) \tag{13}$$

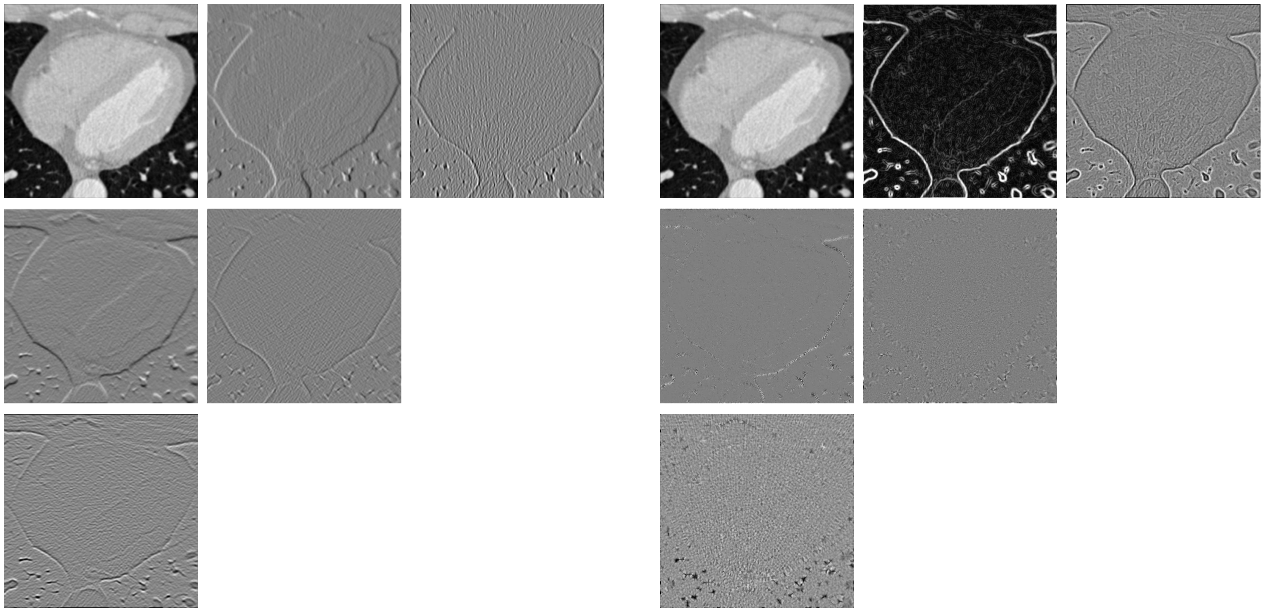

Figure 3. Cartesian (left) and steered (right) Hermite coefficients for $N = 2$ ($n = 0, 1, \ldots, N$ and $m = 0, 1, \cdots, n$) of slice 52 of the CT sequence at 20% of the cardiac cycle.

$$\begin{bmatrix} L_{0,0} & L_{1,0} & L_{2,0} \\ L_{0,1} & L_{1,1} & \\ L_{0,2} & & \end{bmatrix}(x, y) \qquad \begin{bmatrix} L_{0,0} & l_{1,0,\theta} & l_{2,0,\theta} \\ l_{0,1,\theta} & l_{1,1,\theta} & \\ l_{0,2,\theta} & & \end{bmatrix}(x, y)$$

Filters of increasing order n analyze successively higher radial frequencies (Fig. 2 (left)) and filters of the same order n and different (directional) index m distinguish between different orientations in the image.[2] Note that the radial frequency selectivity $d_n(\omega)$ is the same for all $N + 1$ filters of the order n and that these filters differ only in their orientation selectivity.

In order to obtain the steered Hermite coefficients, the Hermite coefficients are rotated toward the estimated local orientation, according to a criterion of maximum oriented energy at each window position. For local 1D patterns, the steered Hermite transform provides a very efficient representation. This representation consists of a parameter θ that indicates the orientation of the pattern and a small number of coefficients that represent the profile of the pattern perpendicular to its orientation. For patterns that are locally 1D, steering over θ results in a compaction of energy into the coefficients $l_{0,n,\theta}(x, y) = l_{n,\theta}(x, y)$, while all other coefficients are set to zero. This means that a steered Hermite transform offers a way to describe 1D patterns explicitly on the basis of their orientation and profile.[16]

In Fig. 3 (right) we steer the cartesian Hermite coefficients according to maximum energy direction, the angle θ was estimated using the phase of the gradient, which is a good indicator of the direction of the edges, for this we use the coefficients L_{01} and L_{10} which are a good approach to optimal edge detectors in the horizontal and vertical directions respectively. It is noticeable that the energy is concentrated in only three coefficients, which represent the orientation of the different structures of the image.

3. OPTICAL FLOW ESTIMATION

Optical flow estimation is still one of the key problems in computer vision. Estimation of the displacement field between two images, applies in those situations requiring the correspondence between the pixels of an image to another.

The optical flow (OF) can be defined as 2D distribution of apparent velocities that can be associated with a variation of brightness patterns in a sequence of images. It can be represented by a vector field induced by the motion of objects (or sensor), which encodes the displacement of each pixel in the image.

Let $L(x, y, t)$ be a image sequence, where (x, y) represents the location within a rectangular image domain Ω, and $t \in [0, \tau]$ denotes time. Let u and v be the displacement of a pixel at position (x, y) within the sequence of images at a time t to a time $(t + 1)$ in the directions x and y respectively.

The *Optical Flow Constraint* proposed by Horn and Schunck[17] in 1981 assumes that the intensities of the pixels of the objects remain constant (*Constant Intensity Constraint*) and is valid when the displacements are relatively small (linear):

$$uL_x + vL_y + L_t = 0 \tag{14}$$

where $L_* := \frac{\partial L}{\partial *}$.

As the intensity does not always remain constant from one image to another an independent intensity change measure is required. In Nagel H.–H. (1983)[18] and Nagel H.–H. and Enkelmann (1986)[19] a *Constant Gradient Constraint* is proposed:

$$\nabla L(x + u, y + v, t + 1) - \nabla L(x, y, t) = 0 \tag{15}$$

Eq. (14) is not sufficient to determine the two unknown functions u and v uniquely (aperture problem). In order to recover a unique flow field, an additional constraint is therefore required. Horn and Schunck[17] assumes that the apparent speed of the intensity pattern in the image varies smoothly, that is, neighboring points of the objects have similar velocities (*Uniform Smoothness Constraint*):

$$\int_\Omega \left(|\nabla u|^2 + |\nabla v|^2 \right) dxdy = 0 \tag{16}$$

In general, regularization–based optic flow methods[20] assume that the optical flow field should be smooth (or at least piecewise smooth). In Horn and Schunck[17] the basic idea is to recover the optical flow as a minimizer of the energy functional:

$$E(u, v) = \int_\Omega \left((uL_x + vL_y + L_t)^2 + \alpha \left(|\nabla u|^2 + |\nabla v|^2 \right) \right) dxdy \tag{17}$$

The first term in Eq. (17) is a data term requiring that the *Optical Flow Constraint* equation be fulfilled, while the second term penalizes deviations from (piecewise) smoothness. The positive smoothness weight α is the regularization parameter.

The *Uniform Smoothness Constraint* used in Horn and Schunck[17] in Eq. (17) causes an over–smoothing at borders of objects, creating blurry optic flow fields, smoothing in a completely homogeneous way.

In order to reduce smoothing at motion boundaries, one may consider using a flow–driven regularizer:[20]

$$E(u, v) = \int_\Omega \left((uL_x + vL_y + L_t)^2 + \alpha\Psi \left(|\nabla u|^2 + |\nabla v|^2 \right) \right) dxdy \tag{18}$$

where $\Psi\left(s^2\right)$ is a differentiable and increasing smooth function that is convex in s.

The Eq. (14) is valid when the displacements are relatively small. In order to handle large displacements multiresolution strategies are used.[21] In this regard Papenberg et al. (2006)[22] proposes a functional that combines *Constant Intensity Constraint*, *Constant Gradient Constraint*, *Spatio–temporal Smoothness Constraint* and a multiscale (*warping*) non–linear approach:

$$\begin{aligned} E(u, v) = &\int_\mho \Psi\Big(|L(x + u, y + v) - L(x, y)|^2 + \gamma |\nabla L(x + u, y + v) - \nabla L(x, y)|^2 \Big) dxdy \\ &+\alpha \int_\mho \Psi\Big(|\nabla_3 u|^2 + |\nabla_3 v|^2 \Big) dxdy \end{aligned} \tag{19}$$

where $\Psi\left(s^2\right)$ yields the total variation regularizer, $\nabla_3 u := (u_x, u_y, u_t)^\top$, $\mho = \Omega \times [0, \tau]$ and γ is a weight between the *Constant Intensity Constraint* and the *Constant Gradient Constraint*.

In Moya–Albor et al. (2013)[5] we proposed a functional that included local image constraints using the Hermite transform, our proposal is based on the polynomial decomposition of each of the images using the steered Hermite transform as a representation of the local characteristics of images from an perceptual approach within a multiresolution scheme.

There have been previous approaches to motion estimation based on the Hermite transform. Liu et al. (1997)[23] proposed a method that includes a spatio–temporal filtering using the Hermite transform and generalized motion models, such as the affine model, into a single spatial scale. Silván–Cárdenas and Escalante–Ramírez (2000)[24] defined a directional energy in terms of the 1D Hermite transform coefficients of local projections allowing detection of 1D or 2D spatio–temporal patterns within the 3D stack of images. In Escalante–Ramírez et al. (2004),[25] a spatio–temporal energy based method to estimate motion in an image sequences was presented defining a directional energy in terms of the Radon projections of the Hermite transform.

In Martinez, F. et al. (2011)[26] motion patterns in CT images were characterized using a Local Jet Feature approach, which consists of obtaining an homogenous partition of the frequential spectrum by analyzing the image at different scales, which are then characterized by a map of partial derivatives of different orders. The resulting local jet representation is grouped by similarity and the motion is estimated by searching a particular pixel with the closer Local Jet Feature euclidean distance.

Unlike the above methods of optical flow estimation using the Hermite transform[23–25] and Local Jet Feature in CT cardiac images,[26] the present proposal poses a differential approach to estimation using a bio–inspired image representation model that includes some of the more important properties of the first stages of the human visual system. It has been shown that differential methods offer better optical flow estimations.[27,28] On the other hand the Hermite transform represents a multiresolution decomposition tool that mimics the behavior of retinal ganglion cell receptive fields that can be described using the difference of two Gaussian functions at different scales.[29] The proposed analysis filters form a basis allowing to recover the original image as an interpolation of the transform coefficients with the synthesis filters that are correlated with the analysis filters.

Our global energy functional penalizes deviations from the constancy in the polynomial decomposition of degree N ($n = 1, 2, \cdots, N$) of images including a *Constant Intensity Constraint* and *Steered Hermite Coefficient Constraint* within an non–linear multiresolution approach:

$$\begin{aligned} E(u,v) = &\int_\Omega \Psi\left(\left|L_0(x+u,y+v) - L_0(x,y)\right|^2 + \gamma\Big(\sum_{n=1}^{N}\left|l_{n,\theta}(x+u,y+v) - l_{n,\theta}(x,y)\right|^2\Big)\right) dxdy \\ &+\alpha\int_\Omega \Psi\left(\left|\nabla u\right|^2 + \left|\nabla v\right|^2\right) dxdy \end{aligned} \tag{20}$$

where $\Psi(s^2) = \sqrt{(s^2+\epsilon^2)}$ is the modified $\ell 1^*$–norm presented in[21,30] which is robust in the presence of flow discontinuities.

The proposed functional, includes the coefficient of order 0 ($L_0 = L_{0,0}$) that contains a smoothed version of the original image and the steered Hermite coefficients ($l_{n,\theta}$) up to order N where a global change of intensity of the images on two consecutive times violates the *Constant Intensity Constraint*, which also allows dealing with various phenomena, such as translational and rotational motions. Using the steered Hermite coefficients we obtain rotation invariance.[31] This allows defining local image constraints considering constancy in the polynomial decomposition of images and identifying perceptually relevant visual patterns that represent the most important characteristics of the image.

For the numerical implementation (see Moya–Albor et al.[5]) we defined a fixed–point outer iterative scheme to find a solution for (u, v) of the corresponding Euler–Lagrange equations that satisfy the minimization of Eq. (20). The non–linear terms of the form $f(x + u^{k+1}, x + v^{k+1}) - f(x, y)$ where k represents the outer iteration index are expanded with a 1st order Taylor series. Finally, in order to remove the remaining nonlinearity in the optimization function Ψ we applied a second fixed–point iteration l (inner iteration) for obtaining the increments

Sequence	Angular error (°) Papenberg et al.[22]	Angular error (°) Moya-Albor et al.[5]
Dimetrodon	3.03	**2.70**
Hydrangea	6.94	**6.88**
Rubberwhale	6.61	7.69

Table 1. Angular errors.

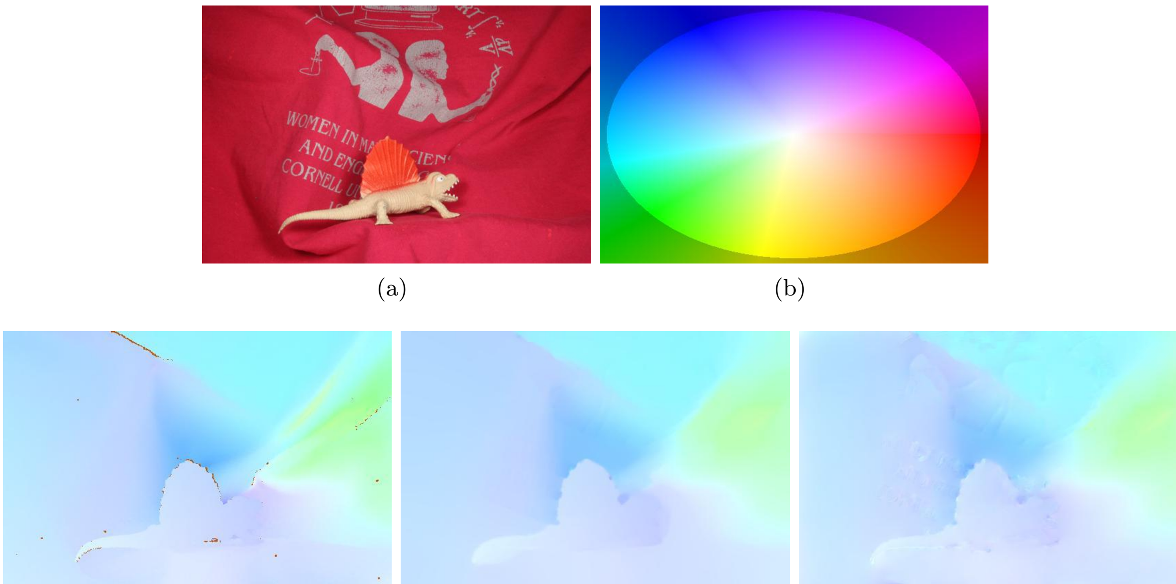

(a) (b)

(c) (d) (e)

Figure 4. Optical flow of the sequence *Dimetrodon*. (a) Frame 10 of the sequence. (b) Reference color wheel. (c) *Ground truth*. (d) Optical flow Papenberg et al. approach.[22] (e) Optical flow using the steered Hermite coefficients.

du^k and dv^k for the outer iteration (k), where $u^{k+1} = u^k + du^{k,l+1}$ and $v^{k+1} = v^k + dv^{k,l+1}$ are the solution for the linear system.

In our approach we use a multiscale strategy[21] allowing that linearization of the corresponding Euler–Lagrange equations be valid. Here a Gaussian pyramid of the image is generated using a downsampling factor $\eta \in (0, 1)$. The coarse images are obtained scaling $L(x, y, t)$ and $L(x+u, y+v, t+1)$ by a factor η^i for $i = M-1, M-2, \cdots, 0$, where M represents the number of decomposition levels.

In order to validate our method we compared our implementation with the 2D algorithm of Papenberg et al.[22] using some sequences of benchmarks of Baker et al. (2007).[32] As a performance measure we calculated the angular error (AE):[32]

$$AE = \arccos\left(\overrightarrow{U_0} \cdot \overrightarrow{U_1}\right) \tag{21}$$

where $\overrightarrow{U_0} = (u_0, v_0)$ and $\overrightarrow{U_1} = (u_1, v_1)$ are two flow normalized vectors and $\{\cdot\}$ represents the dot product.

We obtained the average error from *Dimetrodon*, *Hydrangea* and *Rubberwhale* sequences for both approaches. Table 1 shows the angular error for the approach of Papenberg et al.[22] and through the steered Hermite transform.

In Fig. 4(a) we show the optical flow for the frame 10 of the *Dimetrodon* sequence using the approach of Papenberg et al.[22] (Fig. 4(d)) and the steered Hermite approach (Fig. 4(e)). In order to compare the results in Fig. 4(c) we show the *ground truth* of the displacements. To avoid an overlap between the vectors in the dense optical flow resulting we show the velocity field using a color code (Fig. 4(b)) that encodes the direction (hue) and magnitude (saturation) of the displacement.

Parameter name	Symbol	Value
Hermite Polynomial degree	N	3
Downsampling factor	η	0.95
Regularization parameter	α	50
Local constraint weight	γ	90

Parameter name	Symbol	Value
Decomposition levels	M	40
Outer iteration number	k	15
Inner iteration number	l	50

Table 2. Optical flow parameters using steered Hermite transform approach.

For the optical flow estimation using the steered Hermite transform, we used the parameters of Table 2. These values were obtained by performing several experiments to get the best result in the *Dimetrodon* sequence. Our approach, was implemented in MATLAB® language in a non–optimized code on a workstation PC (Intel Xeon® with 1.8 GHz CPU and 4 GB of RAM), takes about 600 sec to process the optical flow between two consecutive images. For the implementation of Papenberg et al.[22] we used the binaries (calling C++ functions from MATLAB®) of the author's website.[33] Because different languages used is not possible to compare the computational cost of both methods.

4. OPTICAL FLOW ESTIMATION IN CARDIAC CT IMAGES

The heart has been extensively evaluated radiologically, but mostly in standard two–dimensional images (e.g., X–rays and angiograms of the chest). Standard radiographs of the chest (anterior and posterior) may reveal the silhouette of the heart, as well as the great arteries and pulmonary vasculature, but cannot show small structures and easily determine overlapping structures. CT images can be enhanced and manipulated in various ways. Generally an ionized contrast agent is injected intravenously during scanning, allowing smaller structures become visible. Moreover, the data can be reconstructed on the computer to provide images through different planes of the body or three–dimensional images.[34]

The human body can be viewed in three standard anatomic planes, which are oriented perpendicular to each other: sagittal, coronal, and transverse. These planes are aligned with the thoracic midline structures, the aorta and esophagus. In contrast, the heart is oriented obliquely in the chest and therefore imaging in standard anatomic planes is suboptimal to visualize cardiac anatomy and pathology. The heart's three standard planes are its vertical and horizontal long axis and its so–called short axis. These cardiac axes are tilted against the standard anatomic planes.[35]

The axial plane (Fig. 5(a)) is the first image plane in CT and usually gives a good overview of cardiac and coronary anatomy. The long vertical axis (Fig. 5(b)) or two–chamber view is easily produced from the axial plane, this corresponds to a vertical plane through the cardiac apex and the center plane of the mitral valve into the left atrium. This view is adequate to delineate the configuration of the left ventricle and to evaluate contraction of the anterior and lower segment of ventricular left myocardium.[35]

The short axis view is oriented perpendicular to the vertical long axis and is parallel with the mitral valve plane and the cardiac base (Fig. 5(c)). The short axis therefore has a double–oblique angulation to account for the dorsoventral and medioleftlateral tilt of the heart. It can be used to display the right coronary artery down to the cardiac crux, the posterolateral branches of the distal right coronary artery, and the left circumflex coronary artery in its course in the left atrioventricular groove. The left ventricle has a circular aspect on short axis view. Right and left ventricular motion can also be visualized with the short axis view and it is the basis for volumetric measurements used in global ventricular function evaluation.[35]

In this work we use the short axis view which was obtained by applying two spatial transformations using the Amira® software. The parameters of each transformation were obtained by visualizing the data volume and rotating the axial and the coronal axis.

The strongest cardiac movement is found during contraction of the atria and ventricles, i.e., during systole, approximately between 0% and 30% of cardiac cycle. Figs. 6(a) and 6(b) show slice 63 of the short axis view at 0% and 10% of the cardiac cycle (systole) respectively. The resulting optical flow of left ventricle applying the steered Hermite transform approach is shown in Fig. 6(c). In order to isolate the optical flow of the left ventricle

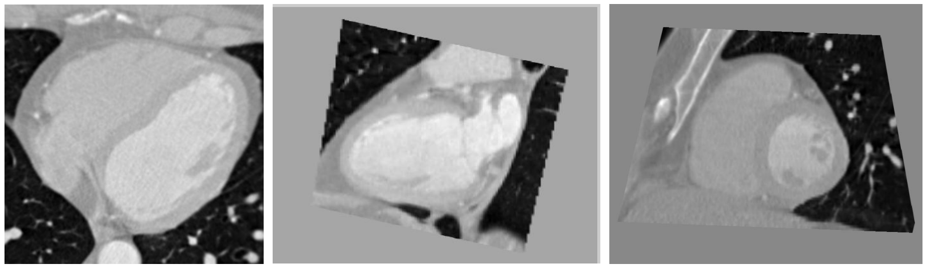

(a) Axial plane (slice 52) (b) Long vertical axis (slice 453) (c) Short axis (slice 63)

Figure 5. The heart's standard planes of CT sequence at 0% of the cardiac cycle.

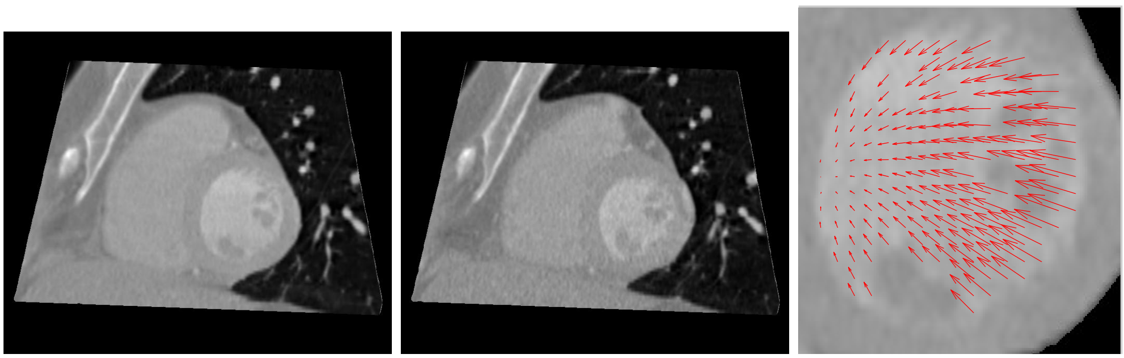

(a) Slice 63 at 0% (b) Slice 63 at 10% (c) *OF* 0–10% of LV

Figure 6. Optical flow estimation of the short axis view between 0–10% of the cardiac cycle.

we applied a basic segmentation scheme using Otsu's binarization, morphological operators and a region growing algorithm.

The movement of relaxation during diastole can be seen between 40% to 60% of the cardiac cycle, Fig. 7(c) show the optical flow of left ventricle between 50% and 60% of cardiac cycle of slice 63 of the short axis view (Figs. 7(a) and 7(b)) using the approach of the steered Hermite transform.

5. CONCLUSIONS

In this work, we have implemented motion estimation of the left ventricle of the short axis view using a bio–inspired approach using the steered Hermite transform model which performs a decomposition of the images into visual patterns that are relevant to the human vision system and mimics some of the more important properties

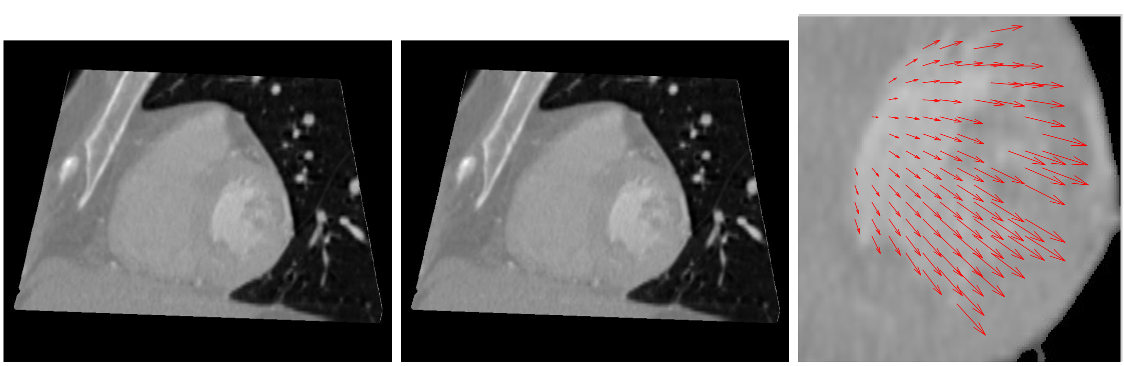

(a) Slice 63 at 50% (b) Slice 63 at 60% (c) *OF* zoom 50–60% of LV

Figure 7. Optical flow estimation of the short axis view between 50–60% of the cardiac cycle.

of early vision such as the behavior of retinal ganglion cell receptive fields. The energy functional used includes a differential approach which incorporates local restrictions and a multiresolution strategy into a non–linear framework.

We used the short axis view of the heart that allows analyzing and visualizing cardiac anatomy and pathology in an optimal plane due to the heart's oblique orientation in the chest. The optical flow allows visualizing the left ventricle in the systole and diastole stage of the cardiac cycle. We calculated the displacements at 0% and 10% of the cardiac cycle where the strongest cardiac movement is present during contraction of the atria and ventricles, i.e., in systole. Also we show the optical flow estimation at 50% and 60% of the cardiac cycle during the movement of relaxation of the heart (diastole). This allows a better visualization of the contraction and relaxation motions of the left ventricle which in turn, may help medical diagnosis.

From a visual examination we notice that our algorithm shows clearer and more defined flows of the contraction and relaxation motions of the left ventricle, being the study of movement of this structure of major importance to physicians.

The segmentation and optical flow estimation of the left ventricle presented in this work constitute a first approximation to understanding the complex heart dynamics. We expect that the accurate optical flow will allow defining an automated motion–based segmentation of the left ventricle walls and obtaining precise quantitative measures of the heart's dynamics by taking advantage of the temporal information.

ACKNOWLEDGEMENTS

This work was supported by UNAM grant PAPIIT IN113611. E. Moya-Albor wish to thank UNAM-CEP for their doctoral scholarship.

REFERENCES

[1] Buckberg, G., Hoffman, J. I. E., Mahajan, A., Saleh, S., and Coghlan, C., "Cardiac Mechanics Revisited: The Relationship of Cardiac Architecture to Ventricular Function," *Circulation* **118**(24), 2571–2587 (2008).

[2] Martens, J.-B., "The Hermite Transform–Theory," *IEEE Transactions on Acoustics, Speech and Signal Processing* **38**(9), 1595–1606 (1990).

[3] Martens, J.-B., "The Hermite Transform–Applications," *IEEE Transactions on Acoustics, Speech and Signal Processing* **38**(9), 1607–1618 (1990).

[4] Young, R. A., "The Gaussian derivative theory of spatial vision: Analysis of cortical cell receptive field line–weighting profiles," Tech. Rep. GMR-4920, General Motors Research Laboratories, Detroit, Mich, USA (1985).

[5] Moya-Albor, E., Escalante-Ramírez, B., and Vallejo, E., "Optical flow estimation in cardiac CT images using the steered Hermite transform," *Signal Processing: Image Communication* **28**(3), 267–291 (2013).

[6] Sakitt, B. and Barlow, H., "A Model for the Economical Encoding of the Visual Image in Cerebral Cortex," *Biological Cybernetics* **43**(2), 97–108 (1982).

[7] Koenderink, J. J. and van Doorn, A. J., "Generic Neighborhood Operators," *IEEE Transactions on Pattern Analysis and Machine Intelligence* **14**(6), 597–605 (1992).

[8] Szegö, G., [*Orthogonal Polynomials*], vol. 53 of *Colloquium Publications*, American Mathematical Society, New York (1959).

[9] Marr, D. C. and Hildreth, E. C., "Theory of Edge Detection," in [*Proceedings of the Royal Society of London*], *B, Biological Sciences* **207**(1167), 187–217 (1980).

[10] Bloom, J. A. and Reed, T. R., "A Gaussian Derivative-Based Transform," *IEEE Transactions on Image Processing* **5**, 551–553 (mar 1996).

[11] Young, R. A., "Simulation of human retinal function with the Gaussian derivative model," in [*Proceedings of the IEEE International Conference on Computer Vision and Pattern Recognition*], 564–569 (1986).

[12] Young, R. A., "The Gaussian derivative model for spatial vision: I. Retinal mechanisms.," *Spatial Vision* **2**(4), 273–293 (1987).

[13] Escalante-Ramírez, B. and Silván-Cárdenas, J. L., "Advanced modeling of visual information processing: A multiresolution directional-oriented image transform based on Gaussian derivatives," *Signal Processing: Image Communication* **20**(9-10), 801–812 (2005).

[14] Silván-Cárdenas, J. L. and Escalante-Ramírez, B., "The Multiscale Hermite Transform for Local Orientation Analysis," *IEEE Transactions on Image Processing* **15**(5), 1236–1253 (2006).

[15] Freeman, W. T. and Adelson, E. H., "The Design and Use of Steerable Filters," *IEEE Transactions on Pattern Analysis and Machine Intelligence* **13**, 891–906 (1991).

[16] van Dijk, A. M. and Martens, J.-B., "Image representation and compression with steered Hermite transforms," *Signal Processing* **56**(1), 1–16 (1997).

[17] Horn, B. K. P. and Schunck, B. G., "Determining Optical Flow," *Artificial Intelligence* **17**(1-3), 185–203 (1981).

[18] Nagel, H.-H., "Constraints for the Estimation of Displacement Vector Fields from Image Sequences," in [*Proceedings of the Eighth International Joint Conference on Artificial Intelligence*], **2**, 945–951 (1983).

[19] Nagel, H.-H. and Enkelmann, W., "An Investigation of Smoothness Constraints for the Estimation of Displacement Vector Fields from Image Sequences," *IEEE Transactions on Pattern Analysis and Machine Intelligence* **8**, 565–593 (September 1986).

[20] Weickert, J. and Schnörr, C., "A Theoretical Framework for Convex Regularizers in PDE-Based Computation of Image Motion," *International Journal of Compututer Vision* **45**, 245–264 (Dec. 2001).

[21] Black, M. J. and Anandan, P., "The Robust Estimation of Multiple Motions: Parametric and Piecewise-Smooth Flow Fields," *Computer Vision and Image Understanding* **63**(1), 75–104 (1996).

[22] Papenberg, N., Bruhn, A., Brox, T., Didas, S., and Weickert, J., "Highly Accurate Optic Flow Computation with Theoretically Justified Warping," *International Journal of Computer Vision* **67**, 141–158 (April 2006).

[23] Liu, H., Hong, T.-H., Herman, M., and Chellappa, R., "A general motion model and spatio-temporal filters for computing optical flow," *International Journal of Computer Vision* **22**, 141–172 (1997).

[24] Silván-Cárdenas, J. L. and Escalante-Ramírez, B., "Optic-flow information extraction with directional gaussian-derivatives," in [*Proceedings of the International Conference on Pattern Recognition*], **3**, 3194–, IEEE Computer Society, Washington, DC, USA (2000).

[25] Escalante-Ramírez, B., Silván-Cárdenas, J. L., and Yuen-zhou, H., "Optic flow estimation using the hermite transform," in [*Proceedings of SPIE in Applications of Digital Image Processing XXVII*], **5558**, 632–643 (2004).

[26] Carrillo, F. M., Manzanera, A., Marta, C. S., and Castro, E. R., "Characterization of motion cardiac patterns in magnetic resonance cine," in [*International Conference on Image Information Processing (ICIIP'11)*], 1–5, IEEE Computer Society, Himachal Pradesh, India (Nov. 2011).

[27] Barron, J. L., Fleet, D. J., and Beauchemin, S. S., "Performance of Optical Flow Techniques," *International Journal of Computer Vision* **12**(1), 43–77 (1994).

[28] Galvin, B., Mccane, B., Novins, K., Mason, D., and Mills, S., "Recovering Motion Fields: An Evaluation of Eight Optical Flow Algorithms," in [*British Machine Vision Conference*], 195–204 (1998).

[29] Rodieck, R., "Quantitative analysis of cat retinal ganglion cell response to visual stimuli," *Vision Research* **5**(12), 583–601 (1965).

[30] Bruhn, A., Weickert, J., and Schnörr, C., "Lucas/Kanade Meets Horn/Schunck: Combining Local and Global Optic Flow Methods," *International Journal of Computer Vision* **61**(3), 211–231 (2005).

[31] Estudillo-Romero, A. and Escalante-Ramírez, B., "Rotation-invariant texture features from the steered Hermite transform," *Pattern Recognition Letters* **32**(16), 2150–2162 (2011).

[32] Baker, S., Scharstein, D., Lewis, J. P., Roth, S., Black, M. J., and Szeliski, R., "A Database and Evaluation Methodology for Optical Flow," *IEEE International Conference on Computer Vision* **0**, 1–8 (2007).

[33] Brox, T., "Classical Variational Optical Flow." `http://lmb.informatik.uni-freiburg.de/resources/binaries` (2011). [accessed 10.12.2011].

[34] Schoenhagen, P., Stillman, A. E., Halliburton, S. S., and White, R. D., "CT of the heart: Principles, advances, clinical uses," *Cleveland Clinic Journal of Medicine* **72**(2), 127–140 (2005).

[35] Fischbach, R., "Cardiac and Cardiothoracic Anatomy in CT," in [*Multi-slice and Dual-source CT in Cardiac Imaging*], 23–39, Springer Berlin Heidelberg, second ed. (2007).